

Response to the Reviewers

Antoon van Hooft, Stéphane Popinet, and Bas van de Wiel

August 2018

The authors thank the reviewers for taking their time to comment on the revised manuscript. The comments of the reviewers are discussed point-by-point. After that, the revised manuscript is presented in a form where all changes made to the old revised manuscript to arrive at the current version of the manuscript have been highlighted.

1 Response to Reviewer #1

We thank the reviewer for the suggested technical corrections.

Figure 8 highlights the diurnal cycles influence on grid refinement. The timing of local midnight or local noon should be noted somewhere.
p.2 Line 17: would be clearer as '..., enabling better resolution of the most demanding processes.'
p.3: C_M and C_H are undefined.
p.8 Line 10: should be 'empiricism'
p.8 Line 15: should be 'Even though'
p.11 Line 2: shouldn't this be Figure 8 not Figure 5?
Figure 1 caption last line: 'several'
Figure 6 caption last line: 'measurement'

We have revised the manuscript accordingly. Noting that we have not changed figure 8 as it already noted the timings of midnight. Furthermore, Eqs. 1a - d introduce C_H and C_M , they are calculated using the definitions of Eqs. 2,3, 5 and 6. (i.e. 2,3,4,5 in the original revised manuscript).

2 Response to Reviewer #2

In the absence of any further comments, this section does not contain a reponse.

3 Response to Reviewer #3

We thank the reviewer for his/hers usefull comments on the revised manuscript. I certainly helped the authors to improve the quality of the work.

Comments from Reviewer 3: The revised manuscript has taken most of my previous comments and questions into consideration. However, the new manuscript has now raised many new questions and concerns, as there are several sign, math and physics errors in the new equations, inadequate descriptions of the test cases and forcing mechanisms, and missing parameter values and undefined symbols. The authors need to provide enough explanations to enable others to repeat the test setups. In case the sign and math errors were present in the computations, all results need to be repeated and reevaluated. This might require major revisions.

The authors agree with most points brought forward by the reviewer and we have therefore revised the manuscript accordingly. We regret that the used closures for the turbulent transport that were added to the first revision were often not written down properly and we again thank the reviewer for his/her review and noticing these errors. It appears we have not been thorough enough when we casted the used formulations in their symbolic mathematical form. For all the issues brought forward regarding the equations were of typographical nature. The correct formulations were in fact already coded in our numerical solver and hence the results do not require an update and we have double checked this. We also hope to adress the other issues raised by the reviewer, both in the new revised manuscript and the point by point response presented below.

1) Eqs. 1a-1d: Using references like Holtslag and Boville (1993), Liu et al. (Mon. Wea. Rev., Feb. 2013) or Andreas and Murphy (J. Physical Oceanography, Nov. 1986), all four surface flux equations 1a-1d have the wrong signs. Explain the sign discrepancy to the aforementioned papers and the sign convention used in this manuscript.

The reviewer is right; we should follow the convection of upward fluxes and we have updated the corresponding equations.

In addition, the definition of q_0 needs to be ‘saturation specific humidity at the surface’. There is a possibility that the surface fluxes have been incorrectly applied in this manuscript, which would necessitate a repetition of all simulations.

In General, the value of the specific humidity at the surface is not necessarily the saturation specific humidity. For some physical scenario’s it would not be an accurate description (e.g. when the soil is drying). For this work we consider its prescription to be a case specific detail, for which we refer to the work of Cuxart et al. (2006) (were $q_0 = 0$) and Svensson et al. (2011). Indeed, for the GABLS2 case it is taken as the saturation specific humidity.

It is also noted that the cited reference Louis (1982) for the surface fluxes does not exist. It is likely that the authors mean the paper Louis et al. (1982): Louis, J.-F., Tiedtke, M, and Geleyn, J.-F.: A short history of the operational PBL parameterization at ECMWF. Proceedings of the Workshop on Planetary Boundary Layer Parameterization, 25-27 November 1981, ECMWF, Reading, U.K., 59-79, 1982 <https://www.ecmwf.int/en/elibrary/10845-short-history-pbl-parameterization-ecmwf> However, this paper does contain any discussion of the surface fluxes (only some exchange coefficients) and is therefore an inadequate reference for the surface fluxes on page 3 line 14. The other provided reference Beljaars et al. (1989) is gray literature (is this an internal technical report, there is insufficient information), it is not available online, and has limited value here. Provide a better reference.

We have updated our references regarding the surface fluxes following the reviewer’s suggestions.

2) Eq. 3: There is again a sign error in this equation. The current formulation wrongly leads to a negative surface-layer bulk Richardson number for stable conditions with $\theta_{v,1} > \theta_{v,1}$. Such a stable stratification needs to have a positive Ri b number (see also Holtslag and Boville (1993), their Eq. (2.8), for the correct definition). Since Ri b is used in Eq. (5), there is the potential that most of the simulations in this manuscript are wrong. This needs to be clarified.

The reviewer is right. we have updated the formulation of the equation in the manuscript. This now also corresponds to how it was already implemented in our model code.

3) Page 4, lines 4 & 5, and Eq, (3): The definition of $\theta_{v,ref}$ is vague. What do you mean by ‘reference value’? Provide the exact definition. Obviously, this reference value of $\theta_{v,ref}$ in the surface layer must be different than the $\theta_{v,ref}$ values used later in the equation for the planetary boundary layer (Eq. (11)). However, the same symbol is used, and no further explanations are offered. Correct this.

$\theta_{v,ref}$ relates the virtual potential temperature (θ_v) to the buoyancy (b), according to the Boussinesq approximation,

$$b = \frac{g}{\theta_{v,ref}} (\theta_v - \theta_{v,ref}).$$

Meaning that for a dry boundary layer, $\theta_{v,ref}^{-1}$ is supposed to be a sufficiently accurate approximation for the thermal expansion coefficient of the air (Bousinesq). As the equations suggest, it is indeed taken as a constant in our model for the ABL, and for the two GABLS cases they are part of the case set-up definition. We have updated the manuscript to be more clear and added an extra reference that provided some inspiration for our implementations. As the reviewer suggests, the approximations are indeed not generally valid and would be one (of many) improvements that would need to be made to have arrived at a more realistic model. We consider this topic to be addressed sufficiently in the manuscript and the previous discussions.

4) Page 4, line 8-9: the capital $Z_{0,M}$ symbol is undefined, needs to be z_0, M . Provide the value of the roughness length to make the results reproducible.

The reviewer is right, it should not have been capitalized. The concept of the roughness length is important for the used closure but its value is typically associated with specific details of the roughness elements at the surface. Therefore, we cannot provide a single value and it is also part of the exact case description of the GABLS1 and GABLS2 cases. If one wishes to reproduce the GABLS cases, it would be required to follow the provided references to the original publications of the GABLS intercomparisons. Also, an unambiguous description of our methods and implementation are documented and freely available online and may be found by following the links in Table 1 or the section labeled ‘code and data availability’ which also includes a tutorial on how to install Basilisk and run the code. As such, we are confident that all our results are reproducible down to the binary-representation precision of a computer.

5) Eq. (9): Incorrect definition of the vertical wind shear magnitude. It needs to read,

$$S_{new} = \sqrt{\left(\frac{\partial u}{\partial z}\right)^2 + \left(\frac{\partial v}{\partial z}\right)^2}$$

instead of the currently used definition

$$S_{old} = \left\| \frac{\partial U}{\partial z} \right\|$$

If the incorrect formulation has been used in the computations, they will need to be repeated.

The reviewer is right and we have updated the manuscript accordingly. Note that we had already implemented the suggested formulation in our computations, also taking into account so-called ‘directional shear’.

6) Eqs. 14, 15, 16: You converted the former vector equation to a scalar equation (as requested) but left the scalar product operator in the formulation. This is mathematically incorrect for the scalar formulation. The dot product needs to be removed. At which time level is the forcing ‘r’ evaluated? Explain (page 6, line 24) that ‘n’ denotes the time level.

The reviewer is right we have updated the manuscript. Which now states that r is integrated in the forward direction, which is indeed an important numerical detail and this warrants a slight textual update as well.

7) section 3.1: The description of the Ekman spiral test is insufficient and needs thorough revisions. It is furthermore unclear how it is correctly implemented. I disagree with the author's reply to my first review that it is not necessary to know the values of the parameters. Without the given values of U_{geo} , f (and thereby the latitude angle φ), Ω , ν , ρ the test case is irreproducible. These values need to be provided.

As mentioned in the text this case bears no resemblance to the planetary ABL, therefore we do not see why the latitude angle on a rotating sphere would need to be introduced. Furthermore, choosing units and corresponding numerical values for f , ν , ρ and U_{geo} becomes highly arbitrary. Remarkably (and fortunately) it appears directly from the (steady) analytical Ekman solution (when written as $u_i(\gamma z)/U_{geo} = f_i(\gamma z)$, with index i a dummy for each direction x, y) is independent from the value of a single dimensionless group defined as e.g. $\Pi = \frac{U_{geo}}{\gamma\nu} = \frac{2U_{geo}\gamma}{f}$. This makes the results particularly reproducible as they are then universal. This in turn means that *any* combination of values for the variables yields the same results when they are properly scaled. We feared that we would risk conveying a different message when listing numerical values for the chosen parameters. Unfortunately, despite our efforts towards this goal, we did not present such properly scaled results as pointed out by the reviewer in the next points. Based on the reviewer's comments we now also realize that the timestepping parameter and the finite machine precision, which appears to influence the results (see discussion below and Fig 1. of this response), does indeed warrant the introduction of the numerical values for reproducibility. Therefore we state that in our set-up we have used normalized values for U_{geo} , f and γ , meaning that $\nu = 1/2$. Note however that the present results are (now) presented in their proper dimensionless form, and that any unit choice for length, time or velocity will yield equivalent results. Noting that the reproducibility of our results is further guaranteed by the fact that our exact methods are documented, shared, mirrored and are freely available (GPL v3 license), see text.

In addition, it needs to be clarified that (a) ν is constant (hidden information via the words 'without any closures', is this correct?) and serves the role of $K(=\nu)$ in Eqs. 14-16

The reviewer is correct, the revised text is now more explicit on K and ν , and that the test case concerns the *laminar* Ekman spiral.

(b) Eqs. (1)-(11) are irrelevant for the discussion

Yes, using these closures is not convenient when the goal is to test consistency of the numerical methods. We would argue that this is sufficiently made clear and motivated in the text that the equations parameterized turbulence in the ABL and that the Ekman spiral case does not concern the ABL.

(c) the exact definition for the forcing terms r needs to be provided for u and v . In order to arrive at the analytical solutions (17) and (18) of the Ekman spiral, it must be assumed that the motion vanishes at $z = 0$ and tends to the zonal geostrophic value $v = U_{geo}$ in the free atmosphere. In addition, the Ekman solution (17) and (18) is based on the equation set

$$0 = K \frac{\partial^2 u}{\partial z^2} + fv - \frac{1}{\rho} \frac{\partial P}{\partial x}$$

$$0 = K \frac{\partial^2 v}{\partial z^2} - fu - \frac{1}{\rho} \frac{\partial P}{\partial y}$$

When comparing this formulation to Eq. (14) identify exactly how the forcing term r represents the forcing from the Coriolis and pressure gradient term in the u and v equations (provide the equations for r_u and r_v). Note that your definition of

$$\frac{dP}{dy} = U_{geo} f \rho$$

seems to have a sign error and might need to read

$$\frac{dP}{dy} = -U_{geo} f \rho$$

if you imply geostrophic balance.

The reviewer is right, and we have revised the manuscript accordingly.

The other problem with section 3.1 is the incorrect definition of γ (line 20) which needs to be

$$\gamma = \sqrt{\frac{f}{2K}} = \sqrt{\frac{2\Omega \sin(\phi)}{2K}} = \sqrt{\frac{\Omega \sin(\phi)}{K}}$$

Only in the very special case of $\phi = \pi/2$ (North Pole) is this equation identical to the definition of γ in the manuscript. However, this is not specified, and γ might be used in an incorrect way

The reviewer is right. We had stated that the equations of motion are evaluated in a rotating frame of reference with angular velocity Ω . We now realize this is confusing and unclear for two reasons. 1) Ω only concerned the rotation of our model around its axis (i.e. the vertical direction), not around the axis that connects the earth's poles. 2) We had not realized that the symbol Ω is typically associated with the earth's rotation speed. As such the manuscript is revised. The revised manuscript now only uses the Coriolis parameter f , and is explicit on how it enters the equations. (see prev. points)

In addition, the authors call the quantity γ 'Ekman depth'. Since the physical units of γ are m^{-1} this is inadequate (it is an inverse). The γ definition is then wrongly used in the definitions of z_{top} (line 22), t_{end} and dt . The physical units do not work out. Divisions by γ are needed instead of multiplications. The wrong use of γ also affects Figs. (1) and (2). The x-axis label Δ/γ must have units of m^2 in the current version (not dimensionless). Figs. 1 and 2 furthermore suggest that $U_{geo} = 1$ m/s was selected in practice. This is the necessary value to represent the upper error limit of 0.25 m/s along the scaled ξ/U_{geo} y-axis in Figs. 1 and 2. Is this assumption correct? All these aspects need to be clarified.

The reviewer is right, we have been inconsistent with the usage of γ and somehow attributed it with the wrong units, alternating between units of length and inverse length, depending on its usage. This is addressed

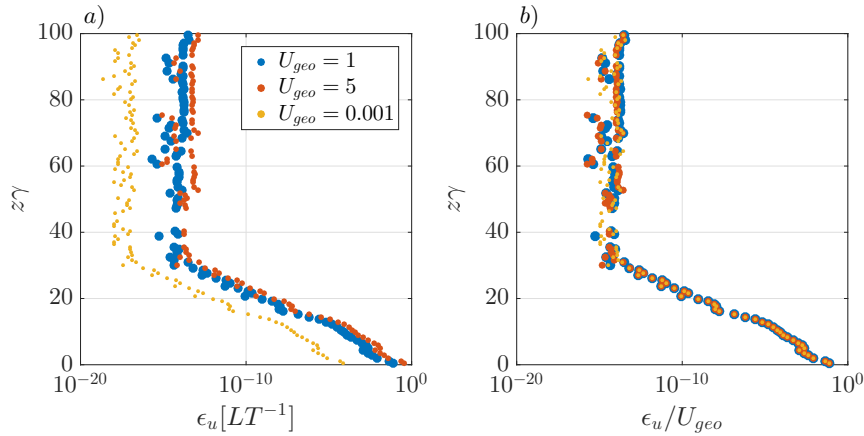


Figure 1: Vertical profiles of the error in the numerically obtained solution (ϵ_u) for the Ekman spiral case at $t = t_{end} = 10/f$ for the run using 128 grid cells. The left hand side (lhs) plot shows the results for runs with three different values for U_{geo} (see legend). Notice the log scale for ϵ_u . The rhs figure plots the same data scaled with the value for U_{geo} to reveal the velocity-scale invariance of our results with respect to it's numerical value. Note that the errors saturate due to the finite precision of the binary representation of numbers.

in the revised manuscript and is now used as an inverse length scale only.

Figs. 1 and 2 furthermore suggest that $U_{geo} = 1$ m/s was selected in practice. This is the necessary value to represent the upper error limit of 0.25 m/s along the scaled ξ/U_{geo} y-axis in Figs. 1 and 2. Is this assumption correct? All these aspects need to be clarified.

A numerical value of 1 for U_{geo} was indeed used (normalized) and we wonder how the reviewer was able to deduce this from the results? The units for velocity (m/s) are arbitrary as nowhere in the text regarding the case set-up, units for length and time are given. Based on the reviewers comments we have added the used values for U_{geo} , f and γ in the revised manuscript. However, we remain certain that the value of $U_{geo} = 1$ is not implied by the results of Fig. 1 and 2. To demonstrate the scale invariance of our results we show the correspondence between the results that would be obtained if one would choose a numerical value for $U_{geo} = 5$ or $U_{geo} = 0.001$. The attached figure shows the diagnosed error ϵ_u for three runs; using $U_{geo} = \{1, 5, 0.001\}$. The domain is discretized using 128 equidistant cells (note that γ and f do not change between the runs). Figure 1 of this response shows vertical profiles of the error and reveals that the values of ϵ_u are higher for the case with the increased wind. However, when we scale the found errors of both runs with the corresponding value for U_{geo} , their values are the same (within machine precision)! This means that our results are representative for an infinite set of runs where U_{geo} is varied. For this non-realistic scenario, we prefer the non-dimensionalized presentation of our results as these values can be easily compared with any simulation result where other values may have been used. We hope this sufficiently clarifies the chosen formulation.

9) Page 8, line 26: how do the 1000 time steps compare to the setting of t_{end} and dt ?

We choose $t_{end} = 10/f$ and $dT = 0.01/f$. The manuscript is now more clear now on this.

10) Section 3.2: Point out that this is a dry test case. It looks as if the GABLS1 case only forces the zonal momentum (line 19). Also add the information about the constant Coriolis parameter f and the density ρ . Does the density vary with height and if yes, how? As in section 3.1, provide the exact forcing functions r_u , r_v and r_θ . It seems clear how Eqs. (6)-(11) connect to Eqs. (14)-(16) (via the computation of K), but it is unclear how the surface flux equations (1)-(5) enter Eqs. (14)-(16). Provide this information.

The reviewer is right and we now also discuss how the surface fluxes enter the computations and how r is formulated in Sect. 2. As for the case descriptions, we have chosen to only provide a brief description of the case and refer to the literature for the details. The density of air does not explicitly enter the equations that are solved in our SCM.

Cuxart et al. (2006) presented their results after 9 hours (averaged over the 9 th hour). You average the results over the 8 th hour and compare to Cuxart et al. (2006). What is the reason for the discrepancy? Are the results converged enough to a steady-state solution that the 8 th and 9 th hour time frames become comparable? Provide an explanation.

The reviewer is right about this flaw, there is no good reason that we presented the 8-th hour average and compare against the 9-th hour average of the LES results of Beare et al. (2006). The GABLS1 case is therefore re-run, for both the equidistant and adaptive grid approaches until $t_{end} = 9h$ to calculate the 9-th hour average. Noting that the resulting profiles for the wind did not change significantly. However, due to the constant cooling rate, the temperature at the surface did change by another 0.25 Kelvin and the near surface results do now *correspond better to the LES results* ... Furthermore, figure 2 now covers the evolution of the grid structure over 9 hours instead of the previous 8 hours and the numbers in table 1 have also been updated. The new results do not warrant any changes to the analysis in the text. We also wanted to visually inspect the steadiness of our solution (and grid), and therefore we have rendered a movie of the evolution of our solution (and grid). The resulting movie is considered nice enough to share and it is available via the link; <https://vimeo.com/284590243>. The soundtrack is composed by Wagner and is added for a dramatic cinematic effect only ;).

11) Page 10, line 25 and Figs. 6a,b: which time snapshot is shown? Add this information to the text and the figure caption. The domain is 4000 m high, but only 1300 m are shown in Fig. 6? Why? How do the solutions compare in the upper domain?

We have added the information regarding the time. For the comparison we follow the analysis of the GABLS2-intercomparison participants as in Svensson et al. (2011). We can only *guess* their motivations; Maybe they were (like us) most interested in the representation of the atmospheric boundary layer and not the free troposphere aloft. Or the variations between the models were small as the SCM has not much dynamics there. Anyhow, as mentioned in the text, we obtained their data from their plots that only covers the ABL, so we cannot compare at higher altitudes. This latter argument does not apply to figure 7, so based on the reviewers comments, we updated *that* caption to state that the profile of U is constant with height for $z > 1200m$.

Correction of typos and style:

Page 1, line 15: ‘... an SCM ...’

Page 2, line 27: ‘... built-in ...’

Page 4, line 14: ‘.. description ...’

Page 5, line 24 and page 7, line 25: ‘... its ...’

Page 6, line 17: ‘... spent ...’

Page 7, line 10: should read ‘... clean setup quantifies numerical errors explicitly and tests the ...’

Page 8, line 2: Bring footnote into the main text

Page 8, line 3: ‘...shows the results of the errors at all levels and ...’

Page 8, line 15: ‘... though...’

Page 8, line 28: ‘... arise in the solution ...’

Page 9, line 1: ‘...and the computational performance ...’

Page 10, line 1: ‘... parameterize ...’

Page 10, line 6: ... on the order of ...’

Page 11, line 2: ‘Fig. 5’ needs to read Fig. 8

Page 11, line 8: ‘... presented a one-dimensional ...’

Caption Fig. 1 and 2: Add the information that the errors are shown at t end (the end of the simulation). Also add: the inset shows the errors for all time steps.

Fig. 3: symbol ‘L’ is undefined

Caption, Fig. 4: ‘... eighth hour ...’. Do u and v stay constant above 275 m?

The revised manuscript has taken all the suggestions into account. Except for the suggestion to add that the inserts of Fig. 1 and 2 show the errors for all time steps. The insert show the same data as is plotted in the main plot, but then for a single run. This was done to prevent that data being obscured by subsequently plotted dots of the other runs, and thereby reveal the full spread of this typical result for a single run.

At the risk of repeating ourselves, we again like to thank the reviewer for bringing forward the discussed issues. We feel He or She has greatly helped to improve the quality of the manuscript.

Adaptive Cartesian Meshes for Atmospheric Single-Column Models, a study using Basilisk 18-02-16

J. Antoon van Hooft¹, Stéphane Popinet², and Bas J.H. van de Wiel¹

¹Delft University of Technology, Department of Geoscience and Remote Sensing, Delft, The Netherlands

²Sorbonne Université, Centre National de Recherche Scientifique, UMR 7190, Institut Jean Le Rond D'Alembert, F-75005, Paris, France

Correspondence: Antoon van Hooft (j.a.vanhooft@tudelft.nl)

Abstract. It is well known that the representation of certain atmospheric conditions in climate and weather models can still suffer from the limited grid resolution that is facilitated by modern-day computer systems. Herein we study a simple one-dimensional analogy to those models by using a Single-Column Model (SCM) description of the atmosphere. The model employs an adaptive Cartesian mesh that applies a high-resolution mesh only when and where it is required. The so-called adaptive-grid model is described and we report on our findings obtained for tests to evaluate the representation of the atmospheric boundary layer, based on the first two GABLS intercomparison cases. The analysis shows that the adaptive-grid algorithm is indeed able to dynamically coarsen and refine the numerical grid whilst maintaining an accurate solution. This is an interesting result as in reality, transitional dynamics (e.g. due to the diurnal cycle or due to changing synoptic conditions) are rule rather than exception.

10 *Copyright statement.* All relevant rights reserved

1 Introduction

Single-Column Models (SCMs) are often used as the building blocks for Global (or General) Circulation Models (GCMs). As such, many of the lessons learned from SCM development can be inherited by GCMs and hence the evaluations of SCMs receive considerable attention by the geoscientific model development community (see e.g. Neggers et al., 2012; Bosveld et al., 2014; Baas et al., 2017). In this work, we present a SCM that employs an adaptive Cartesian mesh that can drastically reduce the computational costs of such models, especially when pushing the model's resolution. The philosophy is inspired by recently obtained results on the evolution of atmospheric turbulence in a daytime boundary layer using three-dimensional (3D) adaptive grids. As promising results were obtained for turbulence-resolving techniques such as Direct Numerical Simulations and Large-eddy Simulation (LES), herein we explore whether similar advancements can be made with more practically oriented techniques for the numerical modelling of the atmosphere. As such, the present model uses Reynolds-averaged Navier-Stokes (RANS) techniques to ~~parametrize~~ parameterize the vertical mixing processes due to turbulence (Reynolds, 1895), as is typical in weather and climate models.

The discussion of limited grid resolution is present in many studies of SCMs and GCMs. A prominent example is the nocturnal cumulus-cloud case (Wyant et al., 2007): whereas a high resolution mesh is required for capturing the processes at the cloud interface, a coarser resolution may be used for the time when the sun has risen and the cloud has been dissolved. More generally speaking, virtually all of the atmospheric dynamics that require a relatively high-resolution grid for their representation in numerical models are localized in both space and in time. The issue is made more difficult to tackle by the fact that their spatio-temporal localization is typically not known a priori (e.g. the height and strength of a future inversion layer). Therefore, the pre-tuned and static-type grids that most operational GCMs use (virtually all) are not flexible enough to capture all dynamical regimes accurately or efficiently. This also puts a large strain on the used closures for the sub-grid scale processes. In order to mitigate this challenge, GCMs that employ a so-called adaptive grid have been explored in the literature. Here the grid resolution adaptively varies in both space and time, focussing the computational resources to where and when they are most necessary. Most notably, the innovative works of Jablonowski (2004), Jablonowski et al. (2009) and St-Cyr et al. (2008) report on the usage of both Cartesian and non-conforming three-dimensional adaptive grids and clearly demonstrate the potential of grid adaptivity for GCMs. Inspired by their works, we follow a 1D SCM approach and aim to add to their findings, using different grid-adaptative formulations and solver strategies. Since SCMs do not resolve large-scale atmospheric circulations, the analysis herein focusses on the representation of the Atmospheric Boundary Layer (ABL).

Over the years, the computational resources that are available to run computer models have increased considerably (Schaller, 1997). This has facilitated GCMs to increase their models' spatial resolution, enabling to ~~better~~ resolve the most demanding processes with increased grid resolutions. However, it is important to realize that the (spatial and temporal) fraction of the domain that benefits most from an increasing maximum resolution necessarily decreases as separation of the modelled spatial scales increases (Popinet, 2011). This is because the physical processes that warrant a higher-resolution mesh are virtually never space filling. E.g. the formation phase of tropical cyclones is localized in both space and time and is characterized by internal dynamics that evolve during the formation process. By definition, with an increasing scale separation, only an adaptive-grid approach is able to reflect the effective (or so-called fractal) dimension of the physical system in the scaling of the computational costs (Popinet, 2011; Van Hooft et al., 2018). This is an aspect where the present adaptive-grid approach differs from for example, a dynamic-grid approach (~~see e.g. Dunbar et al., 2008~~)(Dunbar et al., 2008), that employs a fixed number of grid cells that needs to be predefined by the user. This work employs a similar method for grid adaptation as presented in the work of Van Hooft et al. (2018) on 3D-turbulence-resolving simulations of the ABL. As such, this work is also based on the adaptive-grid toolbox and ~~build-in~~built-in solvers provided by the 'Basilisk' code (<http://basilisk.fr>).

We test our model with the well established cases defined for the first two GABLS intercomparison projects for SCMs. As part of the Global Energy and Water cycle EXchanges (GEWEX) modelling and prediction panel, the GEWEX ABL Study (GABLS) was initiated in 2001 to improve understanding of the atmospheric boundary layer processes and their representation in models. Based on observations during field campaigns, a variety of model cases has been designed and studied using both LES and SCMs with a large set of models using traditional static-grid structures. An overview of the results and their interpretation for the first three intercomparison cases are presented in the work of Holtslag et al. (2013). Here we will test the present adaptive-grid SCM based on the first two intercomparison cases, referred to as GABLS1 and GABLS2. These cases

were designed to study the model representation of the stable boundary layer and the diurnal cycle, respectively. Their scenarios prescribe idealized atmospheric conditions and lack the complete set of physical processes and interactions encountered in reality. At this stage within our research, the authors consider this aspect to be an advantage, as the present SCM model does not have a complete set of ~~parametrizations~~ parameterizations for all processes that are typically found in the operational models (see e.g. Slingo, 1987; Grell et al., 2005)).

This paper is organized as follows, the present SCM is discussed in more detail in Sect. 2. Based on the results from a simplified flow problem, Sect. 3 starts with an analysis of the used numerical methods and the grid adaptation strategy. Model results for ABL-focussed cases that are based on the first two GABLS intercomparison scenarios are also presented in Sect. 3. Finally, a discussion and conclusions are presented in Sect. 4.

2 Model Overview

As we focus on the merits of grid adaptivity in this study on SCMs and not on the state-of-the-art closures for the vertical transport phenomena, we have opted to employ simple and well-known descriptions for the turbulent transport processes. More specifically, the present model uses a stability-dependent, first-order, local, K -diffusivity closure as presented in the ~~seminal~~ works work of Louis et al. (1982) and ~~?~~ Holtslag and Boville (1993). For the surface-flux ~~parametrizations~~ parameterizations we again follow the ~~work of Louis et al. (1982)~~ formulations in the work of Holtslag and Boville (1993). However, to improve the representation of mixing under stable conditions, an alteration is made to the formulation of the so-called stability-correction function under stably-stratified conditions. Based on the work of England and McNider (1995), we use a so-called short-tail mixing function. The used closures for the turbulent transport are summarized next. The upward *surface* fluxes (F) of the horizontal velocity components (u, v), the potential temperature (θ) and specific humidity q are evaluated as:

$$F_u = \underline{C} - \underline{C}_M U_1 u_1, \quad (1a)$$

$$F_v = \underline{C} - \underline{C}_M U_1 v_1, \quad (1b)$$

$$25 \quad F_\theta = \underline{C} - \underline{C}_H U_1 (\theta_1 - \theta_0), \quad (1c)$$

$$F_q = \underline{C} - \underline{C}_H U_1 (q_1 - q_0), \quad (1d)$$

Where U is the wind-speed magnitude and indices 0 and 1 refer the to values at the surface and the first model level, respectively. The surface transport coefficients are,

$$C_M = C_N f_{s,M} (\text{Ri}_b), \quad (2a)$$

$$C_H = C_N f_{s,H}(\text{Ri}_b), \quad (2b)$$

with Ri_b the surface bulk Richardson number, that is defined as,

$$5 \quad \text{Ri}_b = \frac{g}{\theta_{v,\text{ref}}} \frac{z_1 (\theta_{v,0} - \theta_{v,1})}{U_1^2} \frac{z_1 (\theta_{v,1} - \theta_{v,0})}{U_1^2}, \quad (3)$$

where g is the acceleration due to gravity, θ_v is the virtual potential temperature and $\theta_{v,\text{ref}}$ a corresponding reference value that needs to be prescribed. In the absence of liquid water, the virtual potential temperature is related to the potential temperature (θ) and specific humidity (q) according to,

$$\theta_v = \theta \left(1 - \left(1 - \frac{R_v}{R_d} \right) q \right), \quad (4)$$

10 with $R_v/R_d = 1.61$ the ratio of the gas constants for water vapour and dry air (Emanuel, 1994; Heus et al., 2010). The so-called neutral exchange coefficient (C_N) is calculated using,

$$C_N = \frac{k^2}{\ln((z_1 + z_{0,M})/z_{0,M})^2}, \quad (5)$$

with $k = 0.4$ the Von Karman constant, z_1 the height of lowest model level and $z_{0,M}$ is the roughness length for momentum. For the cases studied in this work, the roughness length for heat is assumed to be identical to $z_{0,M}$. The stability correction

15 functions for the surface transport of momentum and heat ($f_{s,M}, f_{s,H}$) are,

$$f_{s,M}(\text{Ri}_b) = \begin{cases} 0, & \text{Ri}_b \geq 0.2, \\ \left(1 - \frac{\text{Ri}_b}{0.2}\right)^2, & 0 \leq \text{Ri}_b < 0.2, \\ 1 - \frac{10\text{Ri}_b}{1 + 75C_N \sqrt{((z_1 + z_{0,M})/z_{0,M}) \|\text{Ri}_b\|}}, & \text{Ri}_b < 0, \end{cases} \quad (6a)$$

$$f_{s,H}(\text{Ri}_b) = \begin{cases} f_{s,M}(\text{Ri}_b), & \text{Ri}_b \geq 0, \\ 1 - \frac{15\text{Ri}_b}{1 + 75C_N \sqrt{((z_1 + z_{0,M})/z_{0,M}) \|\text{Ri}_b\|}}, & \text{Ri}_b < 0, \end{cases} \quad (6b)$$

which conclude the discription-description of the surface fluxes. The vertical flux ($\overline{w'a'}$) of a dummy variable a due to turbulence within the boundary layer is based on a local diffusion scheme and is expressed as,

$$\overline{w'a'} = -K \frac{da}{dz} \frac{\partial a}{\partial z}, \quad (7)$$

where K is the so-called eddy diffusivity,

$$K = l^2 S f(\text{Ri}). \quad (8)$$

l represents an effective mixing length,

$$l = \min(kz, l_{bl}), \quad (9)$$

with l_{bl} is the Blackadar length scale, we use, $l_{bl} = 70m$ (Holtslag and Boville, 1993). S is the local wind-shear magnitude,

$$5 \quad S = \left\| \frac{dU}{dz} \right\| \sqrt{\left(\frac{\partial u}{\partial z} \right)^2 + \left(\frac{\partial v}{\partial z} \right)^2} \quad (10)$$

and $f(\text{Ri})$ is the stability correction function for the vertical flux,

$$f(\text{Ri}) = \begin{cases} 0, & \text{Ri} \geq 0.2, \\ \left(1 - \frac{\text{Ri}}{0.2}\right)^2, & 0 \leq \text{Ri} < 0.2, \\ \sqrt{1 - 18\text{Ri}}, & \text{Ri} < 0, \end{cases} \quad (11)$$

i.e. based on the gradient Richardson number,

$$\text{Ri} = \frac{g}{\theta_{v,ref}} \frac{d\theta_v/dz}{S^2} \frac{\partial\theta_v/\partial z}{S^2}. \quad (12)$$

10 The authors of this work realize that there have been considerable advancements on the representation of mixing under unstable conditions in the past decades, e.g non-local mixing (Holtslag and Boville, 1993) and turbulent-kinetic-energy-based closures (see e.g., Mellor and Yamada, 1982; Lenderink and Holtslag, 2004). Therefore, we would like to note that such schemes are compatible with the adaptive-grid approach and they could be readily employed to improve the physical descriptions in the present model. From an implementations' perspective, those schemes would not require any grid-adaptation specific
15 considerations when using the Basilisk code.

For time integration; we recognize a reaction-diffusion-type equation describing the evolution of the horizontal wind components and scalar fields such as the virtual potential temperature and specific humidity (q). For a variable field $s(z, t)$, we write,

$$\frac{\partial s}{\partial t} = \frac{\partial}{\partial z} \left(K \frac{\partial}{\partial z} s \right) + r. \quad (13)$$

20 Where r is a source term and K is the diffusion coefficient. Using a time-implicit first-order-accurate time discretization for the diffusive term and a explicit time integration for the source term (r), with time step Δt separating the solution s^n and s^{n+1} , this can be written,

$$\frac{s^{n+1} - s^n}{\Delta t} = \frac{\partial}{\partial z} \left(K \frac{\partial}{\partial z} s^{n+1} \right) + r^n. \quad (14)$$

Rearranging the terms we get,

$$\frac{\partial}{\partial z} \left(K \frac{\partial}{\partial z} s^{n+1} \right) - \frac{s^{n+1}}{\Delta t} = - \frac{s^n}{\Delta t} - r^n. \quad (15)$$

To obtain a Poisson-Helmholtz equation, Eq. 15 is solved using a multigrid strategy, employing a finite-volume-type second-order-accurate spatial discretization (Popinet, 2017a, b). The source term r in Eq. 13 is defined using different formulations for the various scalar fields in our model. For θ and q , the source term r concerns the tendency in the lowest grid level due to the surface fluxes (F , see Eqs. 1, r_F) and the effect of large scale synoptic divergence (r_w) according to the vertical velocity w (i.e. prescribed for the GABLS2 case). We write for a dummy variable s ,

$$r_{w,s} = -w \frac{\partial s}{\partial z} \quad (16)$$

For the horizontal velocity components (u, v) the corresponding source terms (i.e. r_F and r_w) are also taken into account and supplemented with the additional source term $r_{\nabla_h P, f}$, that concerns the horizontal pressure-gradient-forcing vector ($-\nabla_h P$) and the Coriolis-force term according to the local Coriolis parameter f . For the horizontal velocity vector $\mathbf{u} = \{u, v, 0\}$ we write,

$$r_{\nabla_h P, f} = \frac{-\nabla_h P}{\rho} + f (\hat{\mathbf{k}} \times \mathbf{u}), \quad (17)$$

where ‘ \times ’ represents the vector outer product operator, ρ is the density of air and $\hat{\mathbf{k}} = \{0, 0, 1\}$ the unit vector in the vertical direction. In this work we adopt the commonly used strategy to introduce a velocity vector that known as the geostrophic wind (U_{geo}) to express $-\nabla_h P$, according to,

$$U_{geo} = \frac{\hat{\mathbf{k}}}{\rho f} \times -\nabla_h P. \quad (18)$$

The most prominent feature of the SCM presented in this work is ~~its ability to dynamically coarsen and refine that it adaptively coarsens and refines~~ the grid resolution based on the evolution of the solution itself. As mentioned in the introduction, the associated grid-adaptation algorithm is the same as ~~was used by Van Hooft et al. (2018). We described in~~ Van Hooft et al. (2018). Here we only briefly discuss the general concept ~~here. For an in-depth quantitative discussion with simplified examples, the reader is referred to the aforementioned paper.~~

Apart from the imperfect representation of the physical aspects of a system in numerical models, additional errors naturally arise due to the spatial and temporal discretization. In general, a finer resolution corresponds to a more accurate solution and a simulation result is considered to be ‘converged’ when the numerically obtained solution and ~~its the~~ statistics of interest do not crucially depend on the chosen resolution. The aim of the grid-adaptation algorithm is to dynamically coarsen and refine the mesh so that the errors due to the spatial discretization remain within limited bounds and to be *uniformly distributed* in both space and time. For our adaptive approach this requires, (1) an algorithm that evaluates a local estimate of the discretization error in the representation of selected solution fields (χ_a for a field ‘ a ’) and (2), a corresponding error threshold (ζ_a) that determines if a grid cell’s resolution is either too coarse (i.e. $\chi_a > \zeta_a$), too fine (i.e. $\chi_a < 2\zeta_a/3$), or just fine. Grid adaptation can then be carried out accordingly and the solution values of new grid cells can be found using interpolation techniques. A cell is refined when the estimated error for at least one selected solution field exceeds it’s refinement criterion and a cell is

coarsened when it is considered to be ‘too fine’ for all selected solution fields. The ‘error estimator’ (χ) is based on a so-called multi-resolution analysis that is formally linked to wavelet thresholding. The algorithm aims to estimate the magnitude of higher-order contributions in the spatial variability of the solution that are not captured by the solver’s numerical schemes.

5 Consistent with the second-order spatial accuracy of the solver’s numerical schemes (Popinet, 2017b), the algorithm employs a second-order accurate wavelet-based error estimate. In practice, grid refinement will typically occur at the locations where the solution is highly ‘curved’, ~~whereas~~ whereas those areas where the solution fields vary more ‘linearly’ in space are prone to coarsening. The error threshold, or so-called refinement criterion ζ , is defined by the user. Noting that similar to the pre-tuning of the fixed-in-time grids as is common in most SCMs, the balance between accuracy and the required computational effort

10 remains at the discretion of the model’s user.

For the cases in this work that focus on the ABL (i.e. in Sect 3.2 and 3.3), the dynamics are governed by the wind ($\mathbf{U} = (u, v)$) and the virtual potential temperature (θ_v), hence we base the refinement and coarsening of the grid on a second-order-accurate estimated error associated with the ~~representation~~ representation of these discretized fields. Based on trial and error, we set the corresponding refinement thresholds,

15 $\zeta_{u,v} = 0.25 \text{ m/s},$ (19)

$\zeta_{\theta_v} = 0.5 \text{ K},$ (20)

for both of the horizontal wind components and virtual potential temperature, respectively. These values are the result of a choice by the authors that aims to strike an arbitrary balance between the accuracy of the solution and the computational effort required to run the model. Note that a similar (arbitrary) balance needs also to be found when static grids are employed. For a

20 simple flow set-up, Sect. 3.1 presents an example convergence study to show the effects of using different refinement criteria on the accuracy of the obtained solutions.

Grid adaptation is carried out each time step. The tree-based anisotropic-grid structure in Basilisk facilitates a convenient basis for the multi-resolution analysis and the subsequent refinement and coarsening of cells at integer levels of refinement. This entails that the spatial resolution can vary by factors of two (Popinet, 2011). For the adaptive-grid runs presented in this

25 paper, the time ~~spent~~ spent in the actual grid assessment and adaptation routines is less than than 5% of the total wall-clock time (see table 1).

~~For time integration; we recognize a reaction-diffusion-type equation describing the evolution of the horizontal wind components and scalar fields such as the virtual potential temperature and specific humidity (q_t). For a variable field $s(z, t)$, we write,~~

$$\frac{\partial s}{\partial t} = \frac{\partial}{\partial z} \cdot \left(K \frac{\partial}{\partial z} s \right) + r.$$

30 ~~Where r is a source term and K is the diffusion coefficient. Using a time-implicit first-order-accurate time discretization with time step Δt separating the solution s^n and s^{n+1} , this can be written,~~

$$\frac{s^{n+1} - s^n}{\Delta t} = \frac{\partial}{\partial z} \cdot \left(K \frac{\partial}{\partial z} s^{n+1} \right) + r.$$

Rearranging the terms we get,-

$$\frac{\partial}{\partial z} \cdot \left(K \frac{\partial}{\partial z} s^{n+1} \right) - \frac{s^{n+1}}{\Delta t} = - \frac{s^n}{\Delta t} - r.$$

To obtain a Poisson-Helmholtz equation. Eq. 15 is solved using a multigrid strategy, employing a finite-volume-type second-order-accurate spatial discretization (Popinet, 2017a, b). Apart from the Ekman-spiral case in Sect. 3.1, the physical time step in the ABL-focussed cases is adaptively varied between 2 sec. and 15 sec. based on the convergence properties of the aforementioned iterative solver. Noting that these values are rather small compared to existing SCMs-GCMs that often employ higher-order-accurate time-integration schemes. Additionally, the correlation of spatial and temporal scales warrants a smaller time step, since the present model employs a higher maximum vertical resolution compared to that of an operational GCM. The solver's second-order spatial accuracy is validated and its performance-scaling the performance is accessed for a simple flow set-up in Sect. 3.1. For the exact details of the model set-ups for the cases presented in this paper, the reader is referred to the case-definition files (in legible formatting). Links are provided to their online locations in table 1.

3 Results

3.1 The Laminar Ekman spiral and grid adaptation

Before we focus our attention on cases that concern the ABL, this section discusses the philosophy of the used grid adaptation strategy based on the analysis of a one-dimensional (1D) laminar Ekman-flow set-up. This simple and clean set-up enables to quantify numerical errors explicitly and test the solver's numerical schemes. The aim of this section is to show that the grid-adaptation strategy and the accompanying refinement criteria provide a consistent and powerful framework for adaptive mesh-element-size selection. Results are presented for both an equidistant-grid and the adaptive-grid approach. The case describes a neutrally-stratified fluid with a constant diffusivity for momentum (K) given by the kinematic viscosity ν and density ρ in a rotating frame of reference with angular-velocity Ω respect to the Coriolis parameter f . A flow is forced by a horizontal pressure gradient $dP/dy = U_{geo} f \rho (-\nabla_b P)$ according to Eq. 18 using $U_{geo} = \{U_{geo}, 0\}$, over a no-slip bottom boundary (located at $z_{bottom} = 0$). Where U_{geo} is a velocity scale that is also known as Assuming that the velocity components converge towards the geostrophic wind There vector for $z \rightarrow \infty$ and vanish at the bottom boundary, there exists an analytical, 1D, steady solution for the horizontal wind components (u_E, v_E component profiles ($u_E(z), v_E(z)$), that is known as the Ekman spiral;

$$u_E = U_{geo} (1 - e^{-\gamma z} \cos(\gamma z)), \quad (21)$$

$$v_E = U_{geo} e^{-\gamma z} \sin(\gamma z), \quad (22)$$

with γ the so-called inverse Ekman depth, $\gamma = \sqrt{\Omega/f}$. We initialize the solution $\gamma = \sqrt{f/(2\nu)}$. We choose numerical values for U_{geo}, γ and f of unity in our set-up and present the results in a dimensionless framework. The solution is initialized according to the exact solution and we set boundary conditions based on Eqs. 21 and 22. Equation 13 is solved numerically for both u and v components without any closures for turbulent transport, on a domain with height $z_{top} = 100 \gamma z_{top} = 100 \gamma^{-1}$. The simulation is run until $t_{end} = 10 \times \gamma / U_{geo} t_{end} = 10 f^{-1}$, using a small time step $dt = 0.01 \times \gamma / U_{geo}$ fixed time step $\Delta t = 0.01 f^{-1}$.

The time step is chosen sufficiently small such that the numerical errors are dominated by the spatial discretization rather than by the time-integration scheme. During the simulation run, discretization errors alter the numerical solution from its exact, and analytically steady, initialization. For all runs, the diagnosed statistics regarding the numerical solutions that are presented in this section have become steady at $t = t_{end}$.

The spatial-convergence properties for the equidistant-grid solver are studied by iteratively decreasing the used (equidistant) mesh-element sizes (Δ) by factors of two and we monitor the increasing fidelity of the solution at $t = t_{end}$ between the runs. Therefore, based on the analytical solution, a local error ($\epsilon_{u,v}$) of the numerically obtained solution (u^n, v^n) within each grid cell is diagnosed and is defined here as:

$$\epsilon_a = \|a^n - \langle a_E \rangle\|, \quad (23)$$

where a is a dummy variable for u and v , $\langle a_E \rangle$ is the grid-cell-averaged value of the analytical solution (a_E) and a^n the value of the numerical solution within the cell¹. Noting that a^n also represents the grid-cell-averaged value in our finite-volume approach. Figure 1a shows the results for all runs and compares the used grid resolution (Δ) with the error $\epsilon_{u,v}$. It appears that the observed range of ϵ -values is large and typically spans 10 orders of magnitude, with a lower bound defined by the ‘machine precision’ (i.e. $\approx 10^{-15}$ for double-precision floating-point numbers). This wide range can be explained by the fact that the Ekman spiral is characterized by exponentially decreasing variation with height (see Eqs. 21, 22) and hence the equidistant grid may be considered overly refined at large z . This illustrates that, for a given solver formulation, the error in the solution is not directly dictated by the mesh-element size, but also depends on *the local shape of the numerical solution itself*. This poses a challenge for the pre-tuning of meshes applied to GCMs, where a balance need to be found between accuracy and computational efficiencyspeed performance. The solution of a future model run is not known beforehand and hence the tuning of the grid typically relies heavily on experience, empiricism and a-priori knowledge. This motivates to apply the method of error *estimation* in the representation of a discretized solution field as described in Popinet (2011) and Van Hooft et al. (2018). For both velocity components, this estimated error ($\chi_{u,v}$) is evaluated at the end of each simulation run for each grid cell and is plotted against the corresponding actual error ($\epsilon_{u,v}$) in Fig. 1b. It seems that for this virtually steady case, there is a clear correlation between the diagnosed (instantaneous) χ -values and the ϵ -values that have accumulated over the simulation run time. Even tough-though the correlation is not perfect, it provides a convenient and consistent framework for a grid adaptation algorithm. As such, a second convergence test for this case is performed using a variable-resolution grid within the domain. The mesh is based on the aforementioned adaptive-grid approach. For these runs, we iteratively decrease the so-called refinement criterion ($\zeta_{u,v}$) by factors of two between the runs and monitor the increasing fidelity of the numerically obtained solution for all runs. The refinement criterion presets a threshold value (ζ) for the estimated error χ that defines when a cell should be refined ($\chi > \zeta$) or alternatively, when it may be coarsened ($\chi < 2\zeta/3$). Figure 2a presents the results and compares the used local grid resolution against $\epsilon_{u,v}$ for the various (colour-coded) runs. It appears that for all separate runs, the algorithm employed a variable resolution mesh and that this has resulted in a smaller range of the local error in the solution (ϵ), as compared to the equidistant-grid cases. The local error in the solution is also compared against the wavelet-

¹ a^n (also) represents the grid-cell-averaged value in a finite-volume approach.

- based estimated error in the representation of the solution fields in Fig. 2b. Compared to the results from the equidistant-grid approach as presented in Fig. 1b), the spread of the χ and ϵ values is relatively small for the separate runs when the adaptive-grid approach is used. The most prominent reason for the finite spread is that the error (ϵ) was diagnosed after 1000 time steps.
- 5 This facilitated errors in the solution that arise in the solution at a specific location (with a large χ -value) to ‘diffuse’ over time towards regions where the solution remains to be characterized by a small χ -value (not shown). Also, since u and v are coupled (due to the background rotation), local errors that arise in the solution for u ‘pollute’ the v -component solution, and vice versa. Furthermore, a spread is expected because the tree-grid structure only allows the resolution to vary by factors of two (Popinet, 2011).
- 10 Finally, the global convergence characteristics and the speed performance of the two approaches are studied. The global error (η) in the numerically obtained solution is evaluated as,

$$\eta = \int_{z_{bottom}}^{z_{top}} (\epsilon_u + \epsilon_v) dz, \quad (24)$$

- In order to facilitate a comparison between the methods, we diagnose the number of used grid cells (N) for the adaptive-grid run. Figure 3a shows that for both approaches the error scales inversely proportional to the used number of grid cells to the
- 15 second power (i.e. second-order spatial accuracy in 1D). The adaptive grid results are more accurate than the results from the fixed-grid approach when employing the same number of grid cells. Figure 3b shows that for both approaches the required effort (i.e. measured here in wall-clock time) scales linearly with the number of grid cells, except for the runs that require less than one-tenth of a second to perform. The plots reveals that *per grid cell* there is computational overhead for the adaptive-grid approach. These results show that the used numerical solver is well behaved.

- 20 The following sections are devoted to testing the adaptive-grid approach in a more applied SCM scenario, where the turbulent transport closures are applied (see Sect. 2) and the set-up is unsteady. Here, the quality of the adaptive-grid solution has to be assessed by comparing against reference results from other SCMs, large-eddy simulations and the present model running in equidistant-grid mode.

3.2 GABLS1

- 25 The first GABLS intercomparison case focusses on the representation of a stable boundary layer. Its scenario was inspired by the LES study of an ABL over the Arctic sea by Kosović and Curry (2000). The results from the participating SCMs are summarized and discussed in Cuxart et al. (2006), for the LES intercomparison study, the reader is referred to the work of Beare et al. (2006). The case prescribes the initial profiles for wind and temperature, a constant forcing for momentum corresponding to a geostrophic wind ~~of $U_{geo} = 8$ m/s and vector, $U_{geo} = \{8, 0\}$ m/s and Coriolis parameter $f = 1.39 \times 10^{-4} \text{s}^{-1}$. Furthermore,~~
- 30 a fixed surface-cooling rate of 0.25 K/hour is applied. The model is ~~set-up accordingly, run~~ with a maximum resolution of 6.25 meter and a domain height of 400 meters. The maximum resolution corresponds to 6 levels of tree-grid refinement, where each possible coarser level corresponds to a factor of two increase in grid size.

Due to the idealizations in the case set-up with respect to the reality of the field observations, the model results were not compared against the experimental data (Cuxart et al., 2006). However, for the SCMs, a reference was found in the high-fidelity LES results that tended to agree well between the various models. The LES results therefore serve as a benchmark for the results obtained with the present model. This facilitates a ~~straight-forward~~straightforward testing of the formulations and implementations of the used physical closures, before we continue our analysis towards the full diurnal cycle. Inspired by the analysis of Cuxart et al. (2006) and *their* figure 3, we compare our SCM results with the 6.25 meter-resolution LES ensemble results. We focus on the profiles for the wind components and potential temperature averaged over the ~~eighth~~ninth hour of the simulation in Fig. 4. We observe that the present SCM is in good agreement with the LES results and is able to capture the vertical structure of the ABL, including the low-level jet. The differences are only minor compared to the variations in the results presented in the aforementioned GABLS1 SCM reference paper.

Note that in general, results are of course sensitive to the closure chosen to ~~parametrize~~parameterize the turbulent transport, in our case given by Eqs.6 and 11. In order to separate between the numerical effects of using grid adaptivity and the chosen physical closures, we define an additional reference case in which we run an *equidistant-grid* SCM. This model run employs a fixed 6.25 meter resolution (i.e with 64 cells), but otherwise identical closures and numerical formulations. I.e. we have switched-off the grid adaptivity and maintain the maximum resolution throughout the domain. We can observe that results between both SCMs are in good agreement but ~~r~~r that minor deviations are present. These discrepancies are ~~in~~on the order of magnitude of the refinement criteria and can be reduced by choosing more stringent values, that would result in using more grid cells. The evolution of the adaptive-grid structure is shown in Fig. 5 a. We see that a relatively high resolution is employed near the surface, i.e. in the logarithmic layer. Remarkably, without any a priori knowledge, the grid is refined at a height of $150\text{ m} < z < 200\text{ m}$ as the so-called low-level jet develops, whereas the grid has remained coarse above the boundary layer where the grid resolution was reduced to be as coarse as 100 meters. From Fig.5 b we learn that the number of grid cells varied between 11 and ~~22~~24 over the course of the simulation run.

3.3 GABLS2

The second GABLS model intercomparison case was designed to study the model representation of the ABL over the course of two consecutive diurnal cycles. The case is set-up after the observations that were collected on the 23rd and 24th of October, 1999 during the CASES-99 field experiment in Leon, Kansas, USA (Poulos et al., 2002). The case prescribes idealized forcings for two consecutive days that were characterized by a strong diurnal cycle pattern. During these days, the ABL was relatively dry and there were few clouds. The details of the case are described in the work of Svensson et al. (2011) that was dedicated to the evaluation of the SCM results for the GABLS2 intercomparison. Compared to the original case prescriptions, we choose a slightly higher domain size of $z_{top} = 4096$ meters (compared to 4000 m), so that a maximum resolution of 8 meters corresponds to 9 levels of refinement.

In this section we place our model output in the context of the results presented in the work of Svensson et al. (2011), that, apart from the SCM results, also includes the results from the LES by Kumar et al. (2010). To obtain their data we have used the so-called ‘data digitizer’ of Rohatgi (2018). Inspired by the analysis of Svensson et al. (2011) and *their* figures 10 and 11, we

intercompare our results for the wind-speed magnitude ($U = \|\mathbf{u}\|$) and virtual potential temperature profiles at 14:00 local time on the 23rd of October in Fig. 6 a and b, respectively. Here we see that the results obtained with the present SCM fall within the range of the results as were found with the selected models that participated in the original intercomparison. These models also employed a first-order-style turbulence closure and have a lowest model-level height of less than 5 meters. The present modelled virtual potential temperature (θ_v) shows a slight negative vertical gradient in the well mixed layer. This is a feature related to the usage of the local K -diffusion description for the turbulent transport (see Sect. 2 and the work of Holtslag and Boville (1993)). Figure 6 c presents a timeseries of the 10-meter wind speed (U_{10m}) during the 23-rd of October. Again the present model results compare well with the others. Next, in order to validate the grid-adaptivity independently from the used closures, we present the hourly evolution of the wind speed on the 24-th of October against the results obtained with adaptivity switched off, using 512 *equally-spaced* grid points in Fig. 7. A nearly identical evolution of the wind speed profiles is observed and even the small-scale features in the inversion layer (i.e. $z \approx 800$ m) are present in the adaptive-grid-model calculations. The corresponding evolution of the adaptive-grid structure is presented in Fig. 58, where the colours in the resolution plot appear to sketch a ‘Stullian’ image, showing a prototypical diurnal evolution of the ABL (see figure 1.7 in the book of Stull, 1988). Apparently, the grid-adaptation algorithm has identified (!) the ‘surface layer’ within the convective boundary layer, the stable boundary layer, the entrainment zone and the inversion layer as the dynamic regions that require a high-resolution mesh. Conversely, the well-mixed layer within the CBL, the residual layer and the free-troposphere are evaluated on a coarser mesh. The total number of grid cells varied between 24 and 44.

4 Discussion & Conclusions

In this work we have presented an a one-dimensional (1D) single-column model (SCM) that employs a mesh whose resolution is varied adaptively based on the evolution of the numerically obtained solution. This is an attractive feature because it is a prerequisite to enable the computational effort required for the evaluation of numerical solution to scale with the complexity of the studied physical system. The adaptation algorithm based on limiting discretization errors appears to function very well for a wide variety of geophysical applications: e.g. 3D atmospheric turbulence-resolving models (Van Hooft et al., 2018), tsunami and ocean-wave modelling (Popinet, 2011; Beetham et al., 2016; Marivela-Colmenarejo, 2017), hydrology (Kirstetter et al., 2016), two-phase micro physics (Howland et al., 2016), flow of granular media (Zhou et al., 2017) and shock-wave formation (Eggers et al., 2017). For these studies on highly dynamical systems, the adaptive-grid approach is chosen because it offers a more computationally efficient approach as compared to the usage of static grids.

The present work does not include an in-depth assessment and discussion on the performance of the presented methods in relation to the computational speed. Even though this is an important motivation for the application of the adaptive-grid strategy to GCMs, the authors argue that an a SCM is not suitable for speed-performance testing: the speed of single-column calculations is virtually never a critical issue. Only in 3D mode, when SCMs are ‘stitched together’ to enable the resolving of global circulations, the model’s computational efficiency becomes an issue. Furthermore, the performance of a SCM that employs a few tens of cells is not a good indicator for the performance of a GCM that can employ billions of grid cells. For

the latter, parallel computation overhead and the so-called memory bottle neck are important aspects. In contrast, for the SCM case, the complete instruction set and solution data can typically be loaded onto the cache memory of a single CPU's core. Nevertheless, for the readers' reference, the required run times for the different SCM set-ups presented herein are listed in table 1, and figure 3b also presents quantitative results on this topic and shows that the adaptive-grid solver is well behaved.

5 Following the turbulence resolving study of Van Hooft et al. (2018), the results presented herein are a proof-of-concept for future 3D modelling, using RANS techniques. The authors of this work realize that the present SCM is a far cry from a complete global model and that more research and development is required before the method can be compared on a global-circulation scale. As shown by e.g. Jablonowski (2004), a 3D adaptive grid also allows a variable grid resolution in the horizontal direc-
10 tions. This further enables the computational resources to focus on the most challenging atmospheric processes where there is a temporal and spatial variation in the horizontal-resolution requirement of the grid. Examples include the contrasting dynamics between relatively calm centres of high-pressure circulations and those characterizing stormy low-pressure cells. Also, in the case of a sea breeze event (Arrillaga et al., 2016), it would be beneficial to temporarily increase the horizontal resolution near the land-sea interface. As such, we encourage the usage of this technique for those meteorologically challenging scenarios.

Acknowledgements. The authors gratefully acknowledge the funding by the ERC Consolidator grant (648666). The LES ensemble results
15 used for the GABLS1 intercomparison are kindly made available by Bob Beare; online via: <http://gabls.metoffice.com/> [and we thank three anonymous reviewers for their comments on the manuscript.](#)

Competing interests. The authors declare that there are no competing interests.

Code and data availability. Basilisk is a freely available (GPLv3), multi-purpose tool to solve partial differential equations and has its own website: <http://www.basilisk.fr>. The code contains solvers for Saint-Venant problems, the Navier-Stokes equations, electro hydrodynam-
5 ics and more, see <http://basilisk.fr/src/README>. A selection of examples can be viewed online: <http://www.basilisk.fr/src/examples>. The website also provides general information including; installation instructions and a tutorial. Furthermore, for the work herein, interested readers can visit the model set-up pages and links to their online locations are presented in table 1. The data can easily be generated by running the scripts. Finally, a snapshot of the used code, as it was used in this the work, is made available via ZENODO, with doi link: <https://doi.org/10.5281/zenodo.1203631>.

10 References

- Arrillaga, J. A., Yagüe, C., Sastre, M., and Román-Cascón, C.: A characterisation of sea-breeze events in the eastern Cantabrian coast (Spain) from observational data and WRF simulations, *Atmospheric Research*, 181, 265–280, 2016.
- Baas, P., van de Wiel, B., van der Linden, S., and Bosveld, F.: From Near-Neutral to Strongly Stratified: Adequately Modelling the Clear-Sky Nocturnal Boundary Layer at Cabauw, *Boundary-Layer Meteorology*, pp. 1–22, 2017.
- 15 Beare, R. J., Macvean, M. K., Holtslag, A. A., Cuxart, J., Esau, I., Golaz, J.-C., Jimenez, M. A., Khairoutdinov, M., Kosovic, B., Lewellen, D., et al.: An intercomparison of large-eddy simulations of the stable boundary layer, *Boundary-Layer Meteorology*, 118, 247–272, 2006.
- Beetham, E., Kench, P. S., O’Callaghan, J., and Popinet, S.: Wave transformation and shoreline water level on Funafuti Atoll, Tuvalu, *Journal of Geophysical Research: Oceans*, 121, 311–326, 2016.
- Bosveld, F. C., Baas, P., Steeneveld, G.-J., Holtslag, A. A., Angevine, W. M., Bazile, E., de Bruijn, E. I., Deacu, D., Edwards, J. M., Ek, M.,
20 et al.: The third GABLS intercomparison case for evaluation studies of boundary-layer models. Part B: results and process understanding, *Boundary-layer meteorology*, 152, 157–187, 2014.
- Cuxart, J., Holtslag, A. A., Beare, R. J., Bazile, E., Beljaars, A., Cheng, A., Conangla, L., Ek, M., Freedman, F., Hamdi, R., et al.: Single-column model intercomparison for a stably stratified atmospheric boundary layer, *Boundary-Layer Meteorology*, 118, 273–303, 2006.
- Dunbar, T., Hanert, E., and Hogan, R.: A one-dimensional finite-element boundary-layer model with a vertical adaptive grid, *Boundary-layer
25 meteorology*, 128, 459–472, 2008.
- Eggers, J., Grava, T., Herrada, M., and Pitton, G.: Spatial structure of shock formation, *Journal of Fluid Mechanics*, 820, 208–231, 2017.
- Emanuel, K. A.: *Atmospheric convection*, Oxford university press, 1994.
- England, D. E. and McNider, R. T.: Stability functions based upon shear functions, *Boundary-Layer Meteorology*, 74, 113–130, 1995.
- Grell, G. A., Peckham, S. E., Schmitz, R., McKeen, S. A., Frost, G., Skamarock, W. C., and Eder, B.: Fully coupled “online” chemistry
30 within the WRF model, *Atmospheric Environment*, 39, 6957–6975, 2005.
- Heus, T., van Heerwaarden, C., Jonker, H., Siebesma, A. P., Axelsen, S., van den Dries, K., Geoffroy, O., Moene, A., Pino, D., de Roode, S., and Vilà-Guerau de Arellano, J.: Formulation of and numerical studies with the Dutch Atmospheric Large-Eddy Simulation (DALES), *Geoscientific Model Development*, 3, 415–444, 2010.
- Holtslag, A. and Boville, B.: Local versus nonlocal boundary-layer diffusion in a global climate model, *Journal of Climate*, 6, 1825–1842,
35 1993.
- Holtslag, A., Svensson, G., Baas, P., Basu, S., Beare, B., Beljaars, A., Bosveld, F., Cuxart, J., Lindvall, J., Steeneveld, G., et al.: Stable atmospheric boundary layers and diurnal cycles: challenges for weather and climate models, *Bulletin of the American Meteorological Society*, 94, 1691–1706, 2013.
- Howland, C. J., Antkowiak, A., Castrejón-Pita, J. R., Howison, S. D., Oliver, J. M., Style, R. W., and Castrejón-Pita, A. A.: It’s Harder to Splash on Soft Solids, *Physical review letters*, 117, 184 502, 2016.
- Jablonowski, C.: *Adaptive grids in weather and climate modeling*, Ph.D. thesis, University of Michigan, 2004.
- 5 Jablonowski, C., Oehmke, R. C., and Stout, Q. F.: Block-structured adaptive meshes and reduced grids for atmospheric general circulation models, *Philosophical Transactions of the Royal Society of London A: Mathematical, Physical and Engineering Sciences*, 367, 4497–4522, 2009.
- Kirstetter, G., Hu, J., Delestre, O., Darboux, F., Lagrée, P.-Y., Popinet, S., Fullana, J.-M., and Josserand, C.: Modeling rain-driven overland flow: Empirical versus analytical friction terms in the shallow water approximation, *Journal of Hydrology*, 536, 1–9, 2016.

- 10 Kosović, B. and Curry, J. A.: A large eddy simulation study of a quasi-steady, stably stratified atmospheric boundary layer, *Journal of the atmospheric sciences*, 57, 1052–1068, 2000.
- Kumar, V., Svensson, G., Holtslag, A., Meneveau, C., and Parlange, M. B.: Impact of surface flux formulations and geostrophic forcing on large-eddy simulations of diurnal atmospheric boundary layer flow, *Journal of Applied Meteorology and Climatology*, 49, 1496–1516, 2010.
- 15 Lenderink, G. and Holtslag, A. A.: An updated length-scale formulation for turbulent mixing in clear and cloudy boundary layers, *Quarterly Journal of the Royal Meteorological Society*, 130, 3405–3427, 2004.
- Louis, J., Tiedtke, M., and Geleyn, J.: A short history of PBL parameterization at ECMWF, in: paper presented at the Workshop on Planetary Boundary Layer Parameterization, Eur. Cent. For Medium-Range Weather Forecasts, Reading, England, 1982.
- Marivela-Colmenarejo, R.: Numerical Perspective on Tsunami Hazards and Their Mitigation by Coastal Vegetation, Ph.D. thesis, Virginia Tech, 2017.
- 20 Mellor, G. L. and Yamada, T.: Development of a turbulence closure model for geophysical fluid problems, *Reviews of Geophysics*, 20, 851–875, 1982.
- Neggers, R. A., Siebesma, A. P., and Heus, T.: Continuous single-column model evaluation at a permanent meteorological supersite, *Bulletin of the American Meteorological Society*, 93, 1389–1400, 2012.
- 25 Popinet, S.: Quadtree-adaptive tsunami modelling, *Ocean Dynamics*, 61, 1261–1285, 2011.
- Popinet, S.: Time-implicit discretisation of reaction–diffusion equations, <http://www.basilisk.fr/src/diffusion.h>, accessed: 2018-01-01, 2017a.
- Popinet, S.: Multigrid Poisson-Helmholtz solvers, <http://www.basilisk.fr/src/poisson.h>, accessed: 2018-01-01, 2017b.
- Poulos, G. S., Blumen, W., Fritts, D. C., Lundquist, J. K., Sun, J., Burns, S. P., Nappo, C., Banta, R., Newsom, R., Cuxart, J., et al.: CASES-99: A comprehensive investigation of the stable nocturnal boundary layer, *Bulletin of the American Meteorological Society*, 83, 555–581, 30 2002.
- Reynolds, O.: On the dynamical theory of incompressible viscous fluids and the determination of the criterion., *Philosophical transactions of the Royal Society of London*, 56, 40–45, 1895.
- Rohatgi, A.: WebPlotDigitizer, <https://github.com/ankitrohatgi/WebPlotDigitizer>, accessed via the web interface: 2018-01-01, 2018.
- Schaller, R. R.: Moore’s law: past, present and future, *IEEE spectrum*, 34, 52–59, 1997.
- 35 Slingo, J.: The development and verification of a cloud prediction scheme for the ECMWF model, *Quarterly Journal of the Royal Meteorological Society*, 113, 899–927, 1987.
- St-Cyr, A., Jablonowski, C., Dennis, J. M., Tufo, H. M., and Thomas, S. J.: A comparison of two shallow-water models with nonconforming adaptive grids, *Monthly Weather Review*, 136, 1898–1922, 2008.
- Stull, R. B.: An introduction to boundary layer meteorology, vol. 1, Springer Science & Business Media, 670 pp, 1988.
- Svensson, G., Holtslag, A., Kumar, V., Mauritsen, T., Steeneveld, G., Angevine, W., Bazile, E., Beljaars, A., De Bruijn, E., Cheng, A., et al.: Evaluation of the diurnal cycle in the atmospheric boundary layer over land as represented by a variety of single-column models: the second GABLS experiment, *Boundary-Layer Meteorology*, 140, 177–206, 2011.
- Van Hooft, J. A., Popinet, S., Van Heerwaarden, C. C., Van der Linden, S. J. A., de Roode, S. R., and Van de Wiel, B. J. H.: Towards Adaptive 450 Grids for Atmospheric Boundary Layer Simulations, *Boundary-Layer Meteorology*, 167, 421–443, 2018.
- Wyant, M. C., Bretherton, C. S., Chlond, A., Griffin, B. M., Kitagawa, H., Lappen, C.-L., Larson, V. E., Lock, A., Park, S., De Roode, S. R., et al.: A single-column model intercomparison of a heavily drizzling stratocumulus-topped boundary layer, *Journal of Geophysical Research: Atmospheres*, 112, 2007.

Zhou, Y., Lagrée, P.-Y., Popinet, S., Ruyer, P., and Aussillous, P.: Experiments on, and discrete and continuum simulations of, the discharge
455 of granular media from silos with a lateral orifice, *Journal of Fluid Mechanics*, 829, 459–485, 2017.

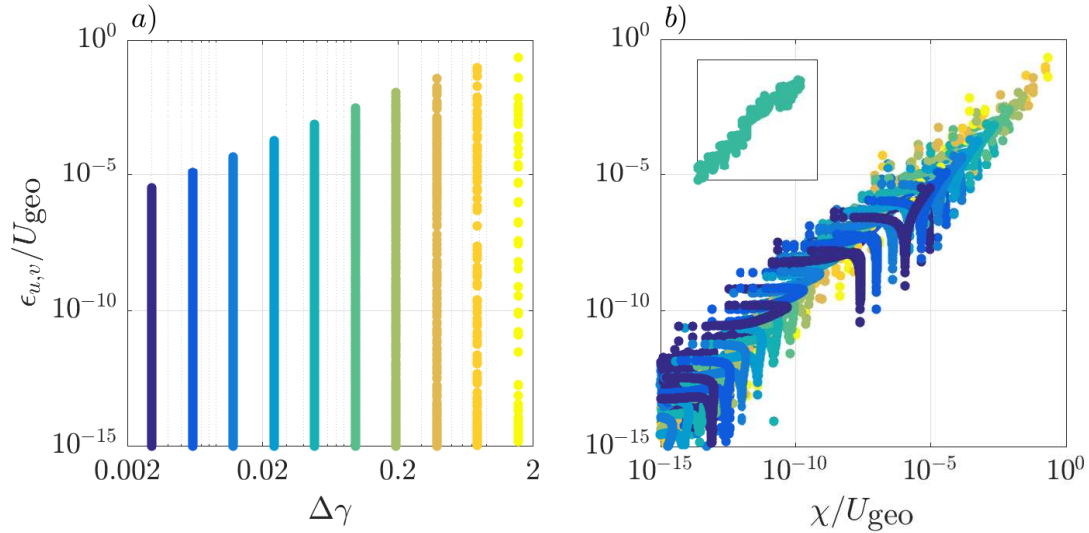


Figure 1. The locally evaluated error in the numerical solutions for u and v at $t = t_{end}$, based on the analytical solution ($\epsilon_{u,v}$, see Eq. 23) for 10 runs with equidistant grids with using different equidistant mesh-element sizes. The left-hand side plot (a) Shows that the diagnosed errors for each run plotted against the used mesh-element size (Δ) times the inverse Ekman depth (γ , see text). The right-hand side plot (b) shows, with the same colour coding as in the left-hand side plot (a), the correlation between the wavelet-based estimated error (χ) and the corresponding diagnosed error in the numerically obtained solution (ϵ). The inset (using the same axis scales) shows the results for a single run, and reveal a spread of several several orders of magnitude in both ϵ and χ values.

Table 1. The exact formulation of the methods are described at the online locations of the definition files for the different cases presented in this manuscript.

Section	Case	Grid	URL: http://www.basilisk.fr...	Number of time steps	Wall-clock time
3.1	Ekman spiral	Adaptive	/sandbox/Antoonvh/ekman.c	1000 ($\times 20$ runs)	≈ 19 sec.
"	"	Fixed & Equidistant	/sandbox/Antoonvh/ekmanfg.c	1000 ($\times 10$ runs)	≈ 18 sec.
3.2	GABLS1	Adaptive	/sandbox/Antoonvh/GABLS1.c	14404 16204	$\approx \del{1.3}1.4 sec.$
"	"	Fixed & Equidistant	/sandbox/Antoonvh/GABLS1fg.c	14404 16324	$\approx \del{0.8}0.9 sec.$
3.3	GABLS2	Adaptive	/sandbox/Antoonvh/GABLS2.c	24262	≈ 9 sec.
"	"	Fixed & Equidistant	/sandbox/Antoonvh/GABLS2fg.c	33993	≈ 22 sec.

The wall-clock times are evaluated using a single core (processor model: Intel i7-6700 HQ).

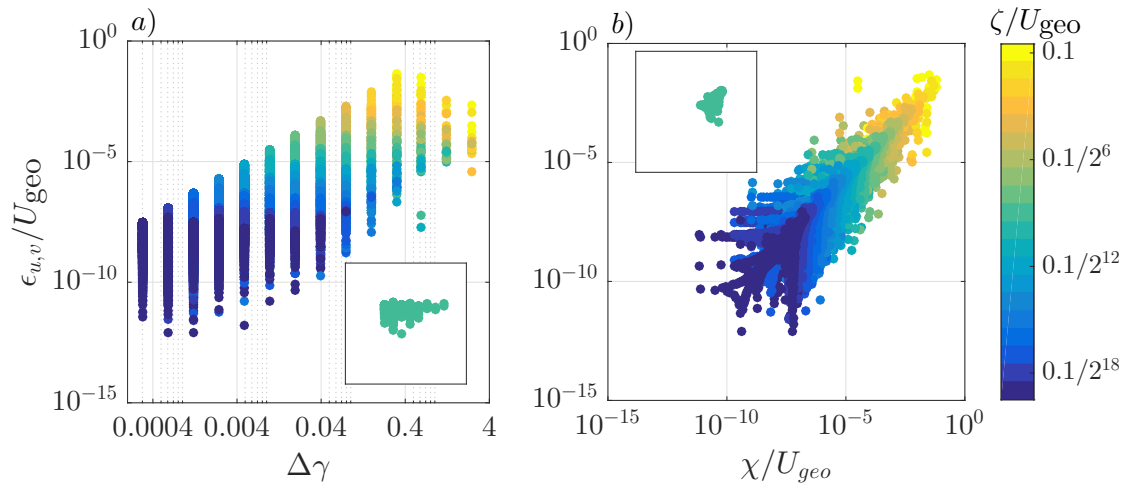


Figure 2. The locally evaluated error in the numerical solutions for u and v at $t = t_{end}$, based on the analytical solution ($\epsilon_{u,v}$, see Eq. 23) for 20 runs using the adaptive-grid approach with different refinement criteria (see [colour bar](#)). The left-hand side plot (a) Shows that the diagnosed errors for each run plotted against the used mesh-element size (Δ). The inset (using the same axis scales) shows the results for a single run. The right-hand side plot (b) shows the correlation between the wavelet-based estimated error (χ) and the corresponding diagnosed error in the numerically obtained solution (ϵ). The inset (using the same axis scales) shows the results for a single run, and reveals a relatively small spread in both ϵ and χ values compared to the equidistant-grid results presented in figure 1b.

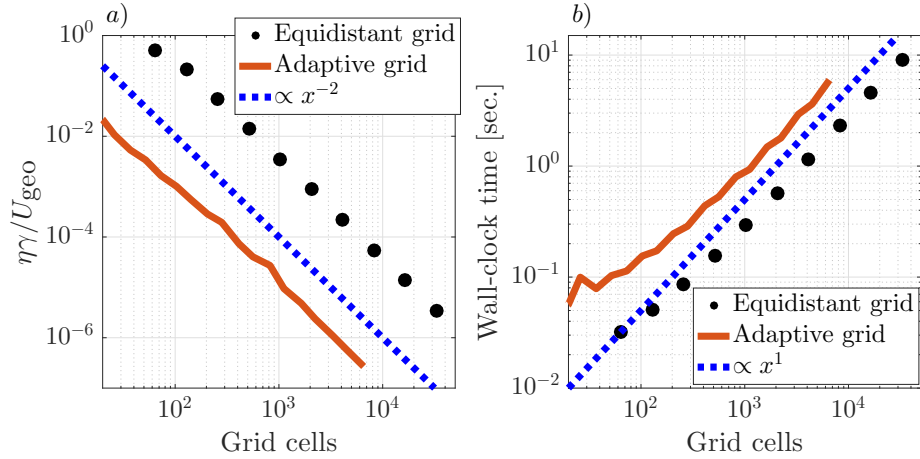


Figure 3. The scaling characteristics for the laminar-Ekman-spiral case. (a) Presents the error convergence for the equidistant-grid and adaptive-grid approach. The errors (η) follow the slope of the blue dashed line that indicates the second-order accuracy of the methods. The wall-clock time for the different runs is presented in (b), showing that for both of the aforementioned approaches, the required effort scales linearly with the number of grid cells.

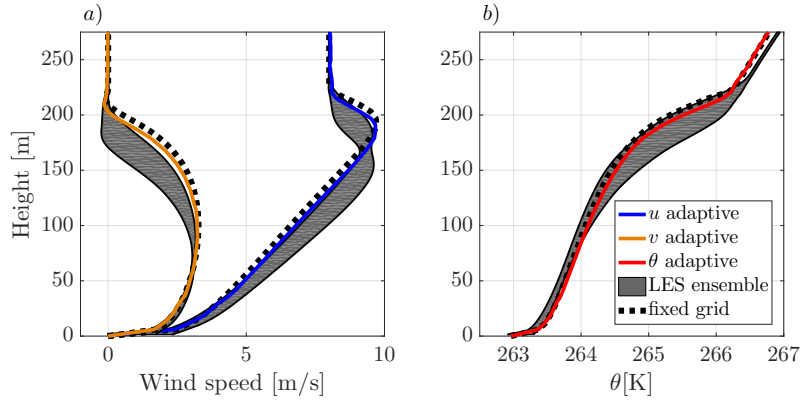


Figure 4. Time averaged profiles over the eight-ninth hour of the run according to the GABLS1 intercomparison scenario. For (a) the horizontal wind components and (b) the potential temperature. Results are obtained with the present adaptive-grid SCM (coloured lines), the LES models ensemble (i.e mean $\pm \sigma$) from Beare et al. (2006) (grey-shaded areas) and the present SCM, employing an equidistant and static grid with a 6.25 meter resolution (dashed lines). For $z > 250\text{m}$, the profiles have remained as they were initialized.

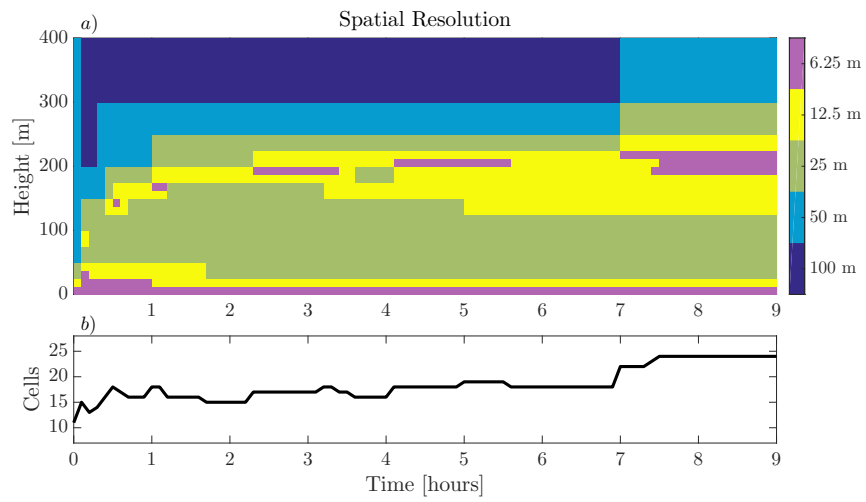


Figure 5. Evolution of (a) the vertical spatial-resolution distribution and (b) the total number of grid cells, for the GABLS1 intercomparison case.

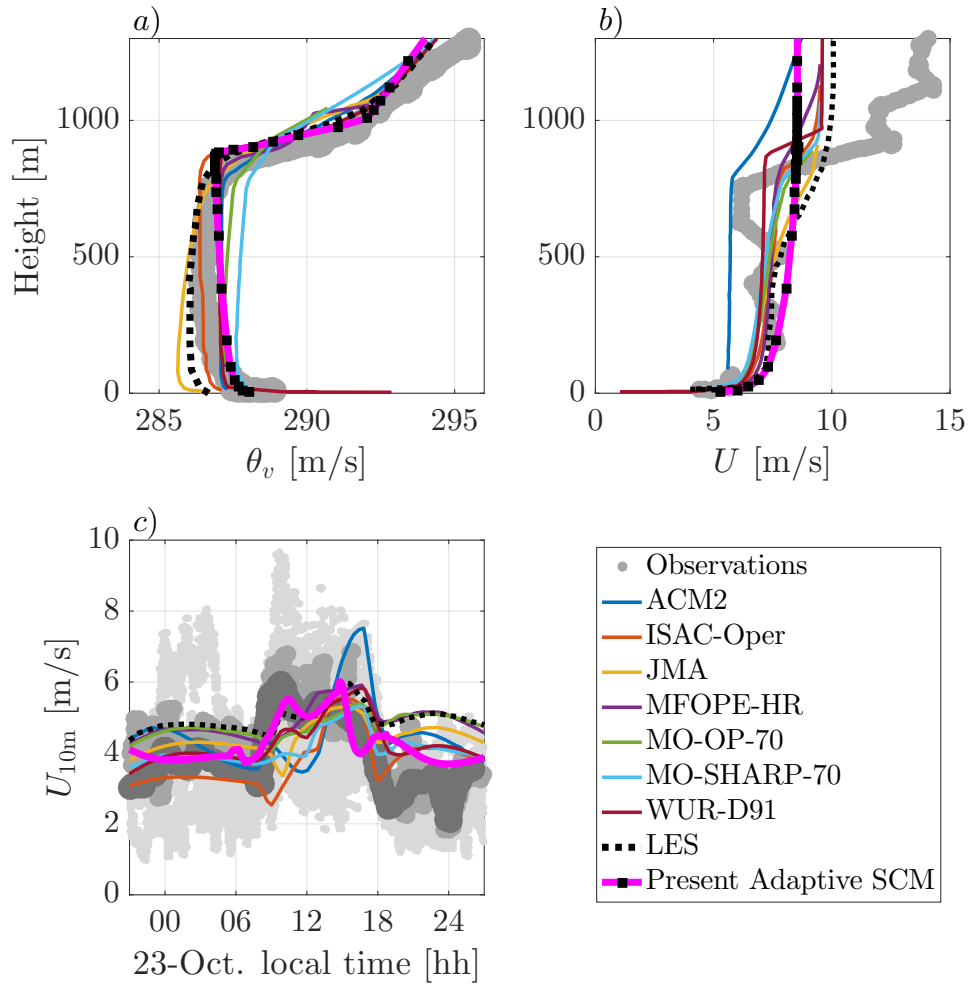


Figure 6. Interecomparison-Comparison of the results obtained with the adaptive-grid SCM and the participating models in the work of (Svensson et al., 2011) for the vertical profiles of (a) the virtual potential temperature and (b) the wind-speed magnitude, for 14:00 local time on the 23rd of October. Lower panel: (c) the evolution of the 10-meter wind speed (U_{10m}) on the 23-th-23rd of October. For the used model abbreviations in the legend, see Svensson et al. (2011). The different shades of grey in plot c) indicate observations from different measurement-measurement devices, see Svensson et al. (2011) for the details.

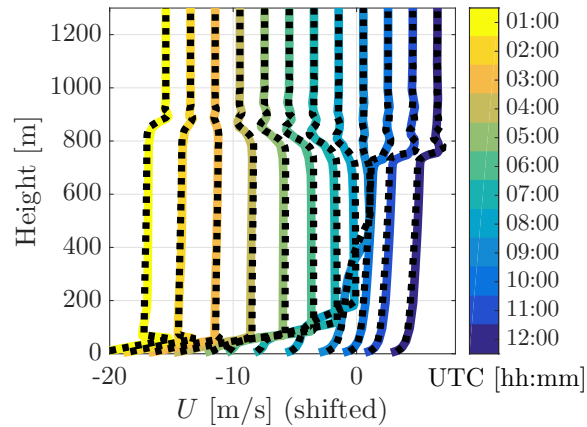


Figure 7. Vertical profiles of the wind-speed magnitude U obtained with the adaptive-grid (in colour) and the fixed equidistant-grid (dashed) SCMs. The twelve plotted profiles are obtained for the 24-th-24th of October with an hourly interval, starting from 1:00 AM local time. Noting that the profiles are shifted in order to distinguish between the different times (with vanishing wind at the surface). The profiles of U are constant with height for $z > 1200\text{m}$.

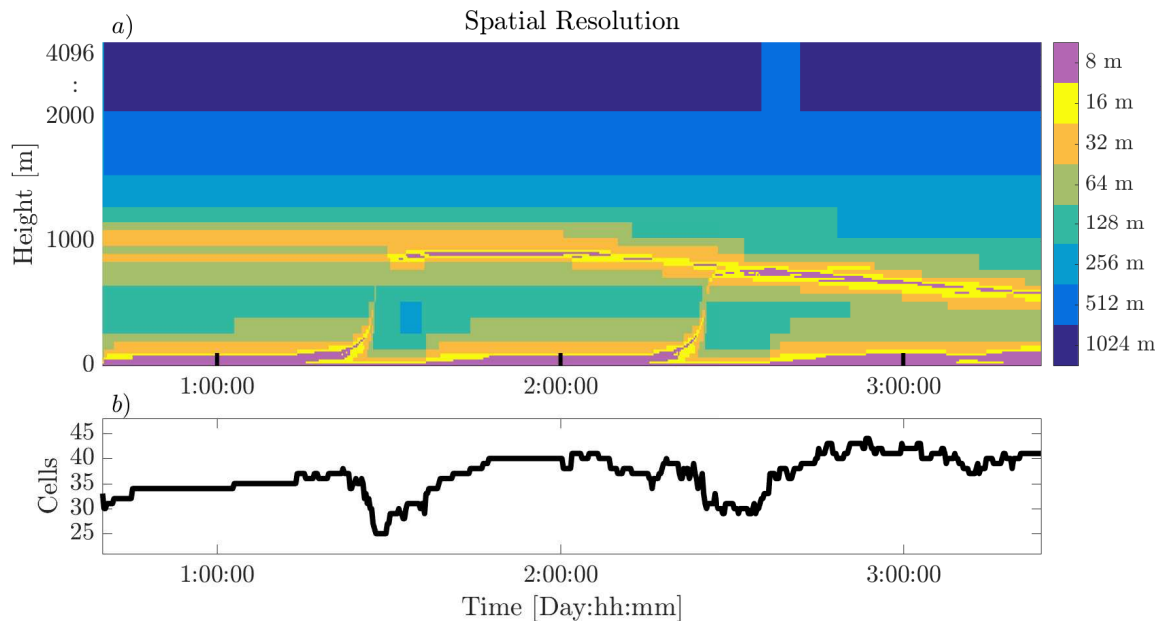


Figure 8. Evolution of (a) the vertical spatial resolution and (b) the total number of grid cells, for the GABLS2 intercomparison case. Two full diurnal cycles, corresponding to the 23-rd-23rd and 24-th-24th day of October, 1999 (ranging from the labels 1:00:00 to 3:00:00 on the x-axis).